Optical Materials 117 (2021) 111091

Contents lists available at ScienceDirect

Optical Materials

journal homepage: www.elsevier.com/locate/optmat

Research Article

Optical properties of in vacuo lithiated nanoporous WO_3:Mo thin films as determined by spectroscopic ellipsometry

Maxime Lagier *, Aurélien Bertinotti, Olivia Bouvard, Luc Burnier, Andreas Schüler

Ecole Polytechnique Fédérale de Lausanne, Solar Energy and Building Physics Laboratory, EPFL LESO-PB, Lausanne, Switzerland

ARTICLE INFO

Keywords:
Electrochromism
Tungsten trioxide
In vacuo lithiation
Vacuum
Sputtering
Spectroscopy
Ellipsometry
Colour neutrality

ABSTRACT

Incorporation of Mo into pure WO_3 thin films is of interest for electrochromic devices, as it improves colour neutrality in the dark state. Existing literature still lacks reliable quantitative data on the complex dielectric function of such coatings. In this study, we deposited WO_3 and $Mo_xW_{1-x}O_3$ thin films by magnetron sputtering and subsequently characterised them by X-ray photoelectron spectrometry (XPS), grazing incidence X-ray diffraction (GIXRD) and scanning electron microscopy (SEM). In vacuo-lithiation was performed to incorporate lithium inside the thin films. The lithiated films were evaluated with variable-angle spectroscopic ellipsometry (VASE) from 340 to 990 nm and with transmission measurements from 330 to 2100 nm. The ellipsometric data were analysed with a straightforward model composed of the sum of Tauc-Lorentz and Lorentz oscillators dispersion laws. One Lorentz oscillator positioned around 1.3 eV is associated with the reduction of W^{6+} to W^{5+} by lithium incorporation. One Lorentz oscillator positioned around 2.3 eV is associated with additional states in the band-gap due to the presence of Mo in the lithiated film. The proposed model allows a better comprehension of the involved electronic transitions and allows to determine the refractive index and extinction coefficient of the materials precisely.

1. Introduction

Electrochromic (EC) materials have increasing prospects in smart windows (controlling solar heat gains or visual comfort), in anti-glare automobile rear view mirrors and in displays due to their low cost and energy consumption [1,2]. When these materials are employed in a suitable device, the optical properties can be modified (clear/dark state) with a relatively small voltage. The process is reversible and caused by insertion/extraction of ions and electrons depending on the polarity of the field [3,4].

An electrochromic device is generally built up from multiple layers. A major colour change can be induced in the cathodic electrochromic layer in order to reach a desired hue. The anodic electrochromic layer can also change colour complementarily to the cathode. An electrolyte, either liquid, gel or solid, is placed between the anodic and cathodic layer; this electrolyte is permeable for the transport of ions but electrically insulating. To complete the device, transparent conductive electrodes are needed to apply a tension, transport the current and carry out the colour changes according to the polarity of the applied voltage.

Tungsten trioxide (WO_3) is among the most studied EC materials serving as an anodic and/or cathodic layer [5–7], and exhibits a colour change when lithium is injected in its lattice following the reaction:

$$WO_3 + xLi^+ + xe^- \rightarrow Li_xWO_3 \quad (1)$$

where WO_3 is transparent and Li_xWO_3 is absorbing. However, a known drawback is that lithiated WO_3 absorbs predominantly yellow, orange and red radiation from the solar spectrum with a maximum absorption around 900 nm and hence appears blue. For many smart window applications, colour neutrality would be preferable.

Recently, M. A. Arvizu and al [4]. showed that the incorporation of a controlled amount of Mo and Ti into the tungsten trioxide leads to colour neutrality and durability, respectively. Other studies also demonstrated colour neutrality combined with good electrochemical and energy storage properties upon Mo insertion [8–10]. But none of them performed a quantitative analysis of the complex dielectric function of lithiated $Mo_xW_{1-x}O_3$ films.

This is specifically what we focus on in this work: we study the effect of Mo insertion on the refractive index and the extinction coefficient of sputtered tungsten trioxide films (WO_3). Measurements by variable-angle spectroscopic ellipsometry (VASE) and spectrophotometry are

* Corresponding author. EPFL/LESO-PB, Station 18, 1015, Lausanne, Switzerland.
E-mail address: maxime.lagier@epfl.ch (M. Lagier).

https://doi.org/10.1016/j.optmat.2021.111091
Received 11 January 2021; Received in revised form 12 March 2021; Accepted 11 April 2021
Available online 8 May 2021

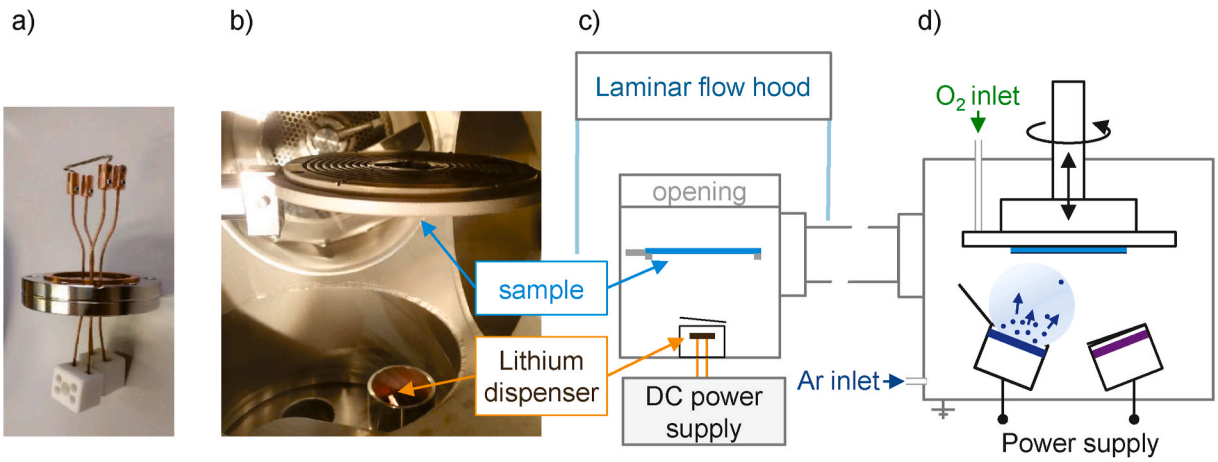

Fig. 1. a) Lithium dispenser installed on an electrical feedthrough b) Lithiation chamber with the sample facing down in the upper part of the image and the lithium dispenser, incandescent, in the lower part c) Schematic of the cluster tool used for the lithiation of the samples and d) for the deposition of thin film coatings by magnetron sputtering.

Table 1
Process parameters. Nanoporous coatings were sputtered at working pressures in the 10^{-2} mbar range. Lower pressure in the 10^{-3} mbar range is suited for compact film deposition.

	WO_3	$Mo_xW_{1-x}O_3$	Lithiation
Target	W	W, Mo	4 x 2 Li dispensers
Applied power	RF 190 W	DC-p 150 W, DC-p 120 W	7.3 A
Deposition time	200 min	140 min	4 x 60 min
Ar/sscm	13	13	–
O_2 /sccm	40	60	–
Working pressure	$1.2{\cdot}10^{-2}$ mbar	$2.7{\cdot}10^{-2}$ mbar	$\sim 10^{-6}$ mbar

analysed using Tauc-Lorentz and Lorentz oscillator dispersion models to derive the optical constants of WO_3 and $Mo_xW_{1-x}O_3$, which leads to a better physical comprehension of the thin films. Complementary characterisation methods such as X-ray diffraction (XRD) and scanning electron microscopy (SEM) are used to determine the morphology and microstructure of the coatings.

Previous studies on pure WO_3 generally use electrochemical processes with liquid electrolytes to insert lithium. In this work, in-vacuo lithiation is performed step-wise, which is more suitable for industrial applications, as it presents the benefit of depositing lithium ions under vacuum in one run, which also means that the thorough cleaning made necessary by the usual electrochemical lithiation can be avoided.

2. Materials and methods

2.1. Thin film deposition

The coatings WO_3 and $Mo_xW_{1-x}O_3$ were deposited by reactive magnetron sputtering in a sputter-up configuration as shown in Fig. 1 from a W (Kurt J Lesker 99.95%) and Mo (Codex-international 99.95%) targets. The setup comprises five magnetrons designed for two-inch targets, which allows thin film deposition by co-sputtering. Bipolar pulsed DC (DC-p) and RF sources have been applied to the targets in argon and oxygen atmosphere. Previously, the deposition parameters had been optimized for RF sources. However, for better compatibility with industrial large scale depositions, DC-p source was later adopted. Powers in the range of 120–190 W were applied to the targets and the deposition time was controlled to obtain similar film thicknesses. To obtain nanoporosity, which is essential for ions extraction in EC devices [11], working pressures in the range of 10^{-2} mbar were used. Glass and single side polished Si (100) substrates were used as host media for the deposited coatings as per the parameters indicated in Table 1.

As shown in Fig. 1 c) d), the sputtering chamber is connected to a transfer chamber in which a lithiation setup was mounted. Lithium dispensers (LI/NF/1.25/25 FT10 + 10, SAES Getters) containing lithium chromate (Li_2CrO_4) are connected to an electrical feedthrough as illustrated in Fig. 1 a). To release lithium from the dispensers, a DC voltage was applied to them, thermally inducing a chemical reaction between lithium chromate ($LiLi_2CrO_4$) and a getter material (Zr–Al 84-16%) [12,13]. Pure alkali deposition can be obtained using these commercial dispensers with low amounts of residual oxygen and hydrogen [13,14]. During the conditioning step, a shutter was used to protect the sample. Then, both WO_3 and $Mo_xW_{1-x}O_3$ underwent 4 lithiation steps in a working pressure range of 10^{-6} mbar (2 dispensers for each lithiation step). Fig. 1 b) shows the sample holder and the lithium dispenser in the transfer chamber during lithiation.

The lithium amount deposited during one lithiation step had been determined in a former study by inductively coupled plasma mass spectrometry (ICP-MS) [11]. Lithium dispensers were emptied on a clean silicon wafer. The thin film was then dissolved by a multi-acidic digestion. The absolute lithium content in the film was measured by ICP-MS and related to the size of the silicon substrate to derive the amount in mol per square centimeters.

2.2. Thin film characterisation

The as-deposited films stoichiometry was determined by X-ray photoelectron spectroscopy (XPS, Mg K_α at $h\nu = 1253.6$ eV), by integrating respectively the 4d, 3d and 1s orbital peaks of W, Mo and O. Film microstructure and morphology were investigated by grazing incidence X-ray diffraction (GIXRD, Empyrean system equipped with PIXcel-1D detector, monochromatic Cu Kα radiation, grazing incidence GI angle 0,8°) and scanning electron microscopy (SEM, Zeiss GeminiSEM 300). VASE (Semilab SE-2000) and UV/Vis/NIR spectrophotometers were used to analyse the optical characteristics of the thin films.

The solar direct transmittance is usually determined from spectra in the full solar range from 250 to 2500 nm. Quick measurements were necessary in this study to reduce the sample oxidation between each lithiation step. As a consequence, we used a Zeiss diode array spectrometer that allows measurements from 350 to 2100 nm. This way, we take into account 97% of the total solar spectrum meaning that the error is less than 3%. The light source is composed of quartz tungsten halogen lamps and UV fluorescence lamps in an aluminium enclosure with a diffusing front glass. A diaphragm is used to ensure light is only

illuminating the sample. Finally a collimator is used to concentrate the transmitted light on an optical fiber, which will lead the light to two diode array spectrometers UV–Vis and NIR (MCS 601 and MCS 611 from Zeiss) [15,16].

Direct transmittance was measured at each successive lithiation step. To do so, the sample had to be taken out of the deposition chamber to conduct measurements and then be placed back in vacuum to undergo the next lithiation step.

The spectral properties of the films were used to determine the coefficient of solar direct transmittance τ_e and light transmittance τ_v using equations (2) and (3) [17].

$$\tau_e = \frac{\sum_{\lambda=350nm}^{2100nm} S_\lambda T(\lambda)\Delta\lambda}{\sum_{\lambda=350nm}^{2100nm} S_\lambda \Delta\lambda} \tag{2}$$

where S_λ is the relative spectral distribution of the solar radiation ASTM G173, $T(\lambda)$ is the spectral transmittance of the glazing and $\Delta\lambda$ is the wavelength interval (in nm).

$$\tau_v = \frac{\sum_{\lambda=380nm}^{780nm} D_\lambda T(\lambda) V(\lambda)\Delta\lambda}{\sum_{\lambda=380nm}^{780nm} D_\lambda V(\lambda)\Delta\lambda} \tag{3}$$

with D_λ being the relative spectral distribution of CIE Standard illuminant D65, $T(\lambda)$ the spectral transmittance of the glazing, $V(\lambda)$ the spectral luminous efficiency for photopic vision defining the standard observer for photometry and $\Delta\lambda$ being the wavelength interval (in nm).

The color coordinates are determined from the visible part of the spectrum (380–780 nm) using the calculations described in the EN410 standard [17].

Spectroscopic ellipsometry is a powerful tool for the characterization of transparent [18] and absorbing [19] thin films. A variable-angle spectroscopic ellipsometer SE-2000 from Semilab working in the spectral range from 340 to 990 nm was used on Si (100) substrates. The Tauc-Lorentz model first derived by Jellison and Modine [20] was used to fit the ellipsometric angles Ψ and Δ from 340 to 990 nm. To model the optical response of thin films in the interband region, the Tauc-Lorentz model has already shown its efficiency [20,21]. The imaginary dielectric function ε_2 exposed in equation (4) is forced to zero below the band-gap. Above the band-gap, four parameters are used in this model, the peak transition energy E_0, the amplitude A, a broadening term C, and the band-gap E_g. Then the real part of the dielectric function ε_1 is obtained by using a Kramers-Kronig relationship, transforming equation (4) into equation (5). This transformation adds a fifth fit parameter $\varepsilon_1(\infty)$.

$$\varepsilon_2(E) = 2nk = \begin{cases} \dfrac{AE_0C(E-E_g)^2}{(E^2-E_0^2)^2 + C^2E^2}\dfrac{1}{E} & E > E_g \\ 0 & E \le E_g \end{cases} \tag{4}$$

$$\varepsilon_1(E) = n^2 - k^2 = \varepsilon_1(\infty) + \frac{2}{\pi} P \int_{E_g}^{\infty} \frac{\xi\varepsilon_2(\xi)}{\xi^2 - E^2} d\xi \tag{5}$$

After lithiation, additional Lorentz oscillators were used to model the absorption below the band-gap due to new electronic states available in the material. The Lorentz oscillator model [22] described in equations (6) and (7), uses three fit parameters: f is the oscillator strength, E_0 is the oscillator position and Γ is the oscillator width. For both models, ε_1 is the real part and ε_2 is the imaginary part of the permittivity.

$$\varepsilon_1(E) = \frac{fE_0^2(E_0^2 - E^2)}{(E_0^2 - E^2)^2 + \Gamma^2E^2} \tag{6}$$

$$\varepsilon_2(E) = \frac{fE_0^2\Gamma E}{(E_0^2 - E^2)^2 + \Gamma^2E^2} \tag{7}$$

Effective medium approximations such as Lorentz-Lorenz, Bruggeman or Maxwell-Garnett models are useful to estimate film porosities [23–25]. This is achieved by comparison of the refractive index of the film to the bulk. In this study the Lorentz-Lorenz effective medium approximation as given in equation (8) was used.

$$p = 1 - \left(\frac{n_f^2 - 1}{n_f^2 + 2}\right) \cdot \left(\frac{n_b^2 + 2}{n_b^2 - 1}\right) \tag{8}$$

where p is the porosity and n_f and n_b are the refractive indices of the film and of the bulk. In this study, n_f was derived from the ellipsometric fits, and the following n_b were taken from literature: $n_{b,550nm}(WO_3) = 2.45$ [26] and $n_{b,550nm}(MoO_3) = 2.52$ [27].

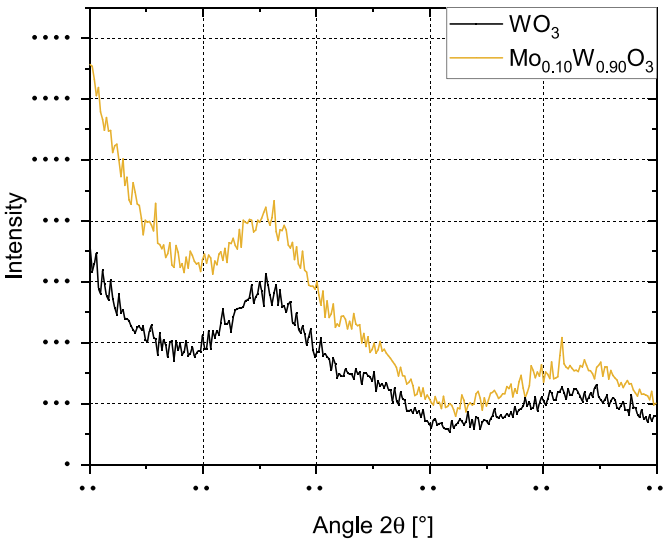

Fig. 2. X-ray diffraction spectra of the WO_3 and $Mo_{0.10}W_{0.90}O_3$ coatings. In both cases, broad peaks are observed, which is typical for amorphous films.

Table 2
Lithium content incorporated into WO_3 and $Mo_{0.10}W_{0.90}O_3$.

Lithiation step	0	1	2	3	4
Li content (x in Li_xWO_3)	0	0.08	0.17	0.25	0.34
Li content (x in $Li_xMo_{0.10}W_{0.90}O_3$)	0	0.11	0.21	0.32	0.42

3. Results

3.1. XPS, ICP MS, GIXRD and SEM characterisation

The as-deposited films underwent several characterisation techniques. Stoichiometry was analysed by XPS measurements and found to be: WO_3 and $Mo_{0.10}W_{0.90}O_3$.

The measured XRD spectra are illustrated in Fig. 2. The black solid line representing pure WO_3 is composed of two broad peaks situated between 20° and 30° and between 45° and 60°. The same observation is made for the yellow solid line representing $Mo_{0.10}W_{0.90}O_3$. The absence of sharp diffraction peaks for both samples is suggesting amorphous structures.

Subsequently, the as-deposited films were lithiated in-vacuo step by step. Between each deposition, the samples were taken out of vacuum to perform transmittance and ellipsometry measurements. The amount of lithium deposited per lithiation step was obtained by ICP MS. It was found to be about $3{\cdot}10^{-7}$ mol·cm^{-2} per lithiation step. Knowing this, the lithium content of each lithiation step represented by the formula Li_xWO_3 and $Li_xMo_{0.10}W_{0.90}O_3$ was calculated as summarised in Table 2.

The film morphology of the as-deposited and lithiated thin films was investigated by Scanning Electron Microscopy. The cross-sections SEM images illustrated in Fig. 3 show a columnar structure growth for all samples and the thickness of each coating has been estimated to be in the

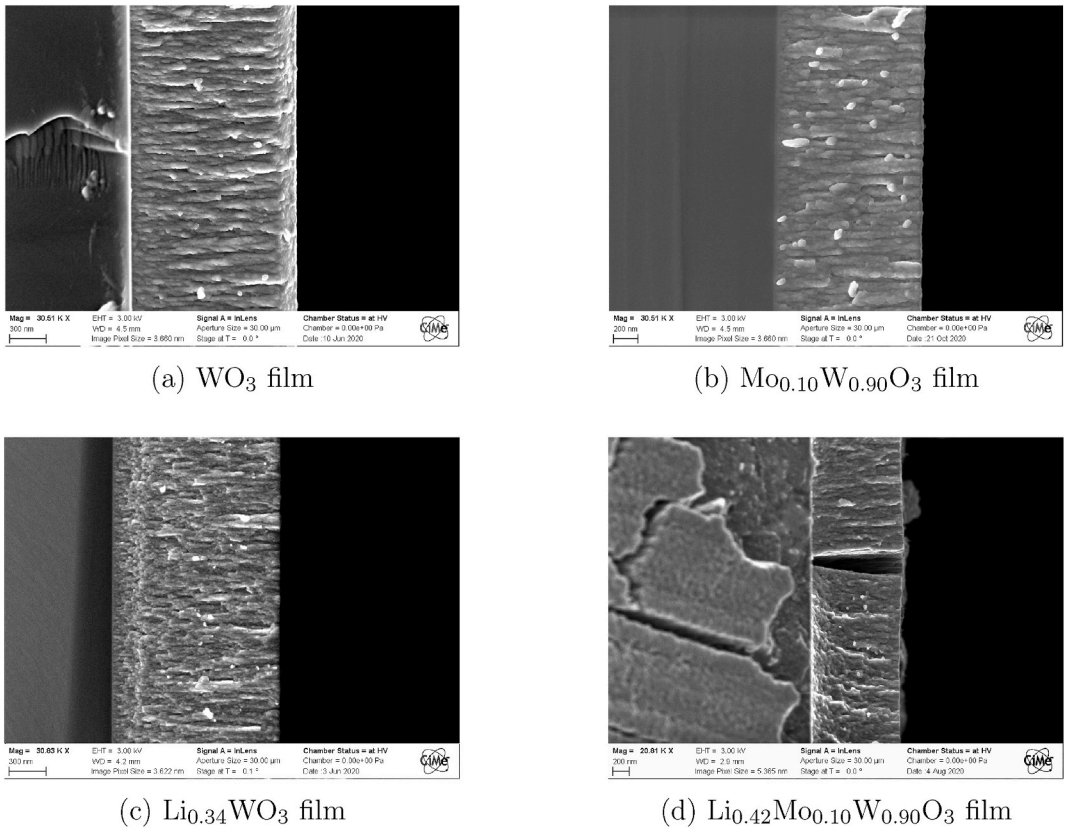

Fig. 3. Cross-section SEM images of the as-deposited and lithiated WO_3 and $Mo_{0.10}W_{0.90}O_3$ coatings. The silicon substrate is situated on the left in all images. A columnar structure growth is observed for all thin films.

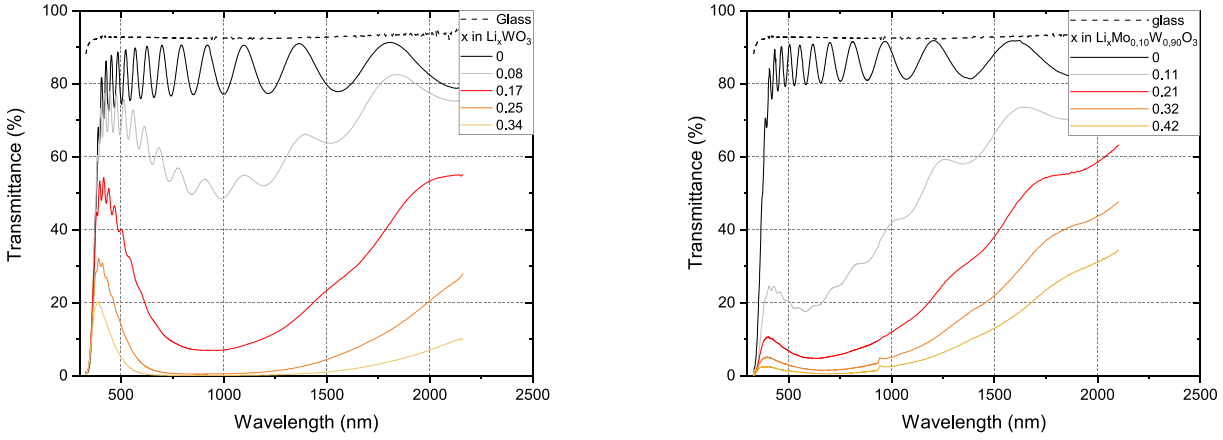

Fig. 4. Spectral transmittance of the WO_3 (left) and $Mo_{0.10}W_{0.90}O_3$ (right) coatings as deposited on glass substrate and after successive lithiations steps. For comparison, the transmittance of the glass substrate is added. Upon lithium insertion, an absorption band centered around 1000 and 630 nm is observed for the WO_3 and $Mo_{0.10}W_{0.90}O_3$ films respectively. The relative flat transmission of $Mo_{0.10}W_{0.90}O_3$ over the visible range explains the neutral colour obtained and depicted in Fig. 5.

order of 1200 ± 200 nm. Additionally, the maximum roughness depth and the arithmetic average roughness *Ra*, for the as-deposited films, have been estimated to be in the order of 30 nm and 7.5 nm respectively, corresponding to approximately 2.5% and 0.6% of the total thin film thicknesses.

3.2. UV-VIS-NIR spectrophotometry

The transmittance of the WO_3 and $Mo_{0.10}W_{0.90}O_3$ films deposited on glass substrates were measured as deposited and after each lithiation step, as shown in Fig. 4. The solar direct transmittance and the light transmittance were calculated for each spectrum and are reported in Table 3.

The spectral transmittance of both samples decreases with an increasing amount of lithium in the films. Indeed, the solar direct transmittance of the as-deposited films is 79.5% and 83.3% respectively for WO_3 and $Mo_{0.10}W_{0.90}O_3$, dropping to 3.3% and 2.7% after the fourth lithiation step. Similarly, the light transmittance of the as-deposited films decreases from 82.2% to 85% respectively for WO_3 and $Mo_{0.10}W_{0.90}O_3$ to 2.2% and 0.9% after the fourth lithiation step.

Table 3
Evolution of solar direct transmittance and light transmittance of WO_3 and $Mo_{0.10}W_{0.90}O_3$ as a function of the content of intercalated lithium.

Lithiation step	Li_xWO_3			$Li_xMo_{0.10}W_{0.90}O_3$		
	x	τ_e	τ_v	x	τ_e	τ_v
0	0	79.5%	82.2%	0	83.3%	85.0%
1	0.08	59.8%	67.9%	0.11	30.4%	18.7%
2	0.17	21.6%	29.2%	0.21	11.2%	5.5%
3	0.25	7.0%	7.4%	0.32	5.2%	2.2%
4	0.34	3.3%	2.2%	0.42	2.7%	0.9%

Furthermore, the values summarised in Table 3 show that a high control of τ_e and τ_v can be obtained as a function of the amount of Li inserted. $Li_{0.34}WO_3$ and $Li_{0.42}Mo_{0.10}W_{0.90}O_3$ underwent both 4 lithiation steps; consequently, the number of inserted lithium atom is approximately the same for both thin films. $Li_{0.42}Mo_{0.10}W_{0.90}O_3$ exhibits a lower light transmittance (τ_v=0.9%) compared to $Li_{0.34}WO_3$ (τ_v=2.2%). Glass coatings with a light transmittance inferior to 1% might be especially preferable to limit glare in the case of direct visibility of the solar disk. Simultaneously $Li_{0.42}Mo_{0.10}W_{0.90}O_3$ exhibits a lower solar direct transmittance (τ_e=2.7%) compared to $Li_{0.34}WO_3$ ((τ_v=3.3%). Such a strong modulation of the solar transmittance would allow an efficient control of solar heat gain in a wide range.

Fig. 4 shows that, for pure WO $_3$, the largest decrease in transmittance occurs in the 600 - 1300 nm range, keeping a relatively high transmittance value in the 380 - 500 nm range. On the other hand, for $Mo_{0.10}W_{0.90}O_3$, the decrease of transmittance is relatively flat over the visible range.

This selectivity is causing a change of perceived colour in the samples. The colour coordinates x and y were determined for each spectra and plotted in the CIE 1931 2°diagram in Fig. 6 (c,d). Additionally, the light transmittances reported in Table 3 were plotted in Fig. 6 (a,b) to illustrate the darkening of the samples. For WO_3, the transmitted colour evolves from transparent to blue. The colour coordinates x and y are respectively evolving from 0.31 to 0.33 to 0.17 and 0.14 after 4 lithiation steps. During the lithium insertion, WO_3 becomes also darker since light transmittance is greatly reduced (about 37 times after the last lithiation step). Concerning $Mo_{0.10}W_{0.90}O_3$, the transmitted apparent colour evolves from transparent to black. The colour coordinates x and y are respectively evolving from 0.31 to 0.33 to 0.24 and 0.25 after 4 lithiation steps. Moreover, an exponential decay of light transmittance is observed for both samples in Fig. 6 (a,b) (directly for $Mo_{0.10}W_{0.90}O_3$ and after 1 lithiation step for WO_3) suggesting a Beer-Lambert relationship between the number of lithium atoms inserted in the sample and the optical transmittance [28].

3.3. Ellipsometric analysis

The ellipsometric data Ψ and Δ have been measured for both WO_3 and $Mo_{0.10}W_{0.90}O_3$ thin films before and after successive lithiation steps at 65, 70 and 75°. Ψ and Δ have also been simulated with Tauc-Lorentz and Lorentz oscillator dispersion laws. In order to illustrate the effect of lithium insertion into the films, the angle of 75° and the lithiation steps 0, 2 and 4 have been selected. The ellipsometric data measured and simulated at these parameters are displayed in Figs. 8 and 9 respectively for WO_3 and $Mo_{0.10}W_{0.90}O_3$. The corresponding fit parameters for simulated data are reported in Tables 4 and 5 for all lithiation steps. The Ψ and Δ data measured and simulated at 65, 70 and 75° are shown for the $Li_{0.08}WO_3$ sample in Fig. 7 showing that the fitting parameters found at 75° are in good agreement for all angles. Roughness is not accounted for the fitting models. The small difference between the measured and simulated data observed in Fig. 7 suggests a small effect of roughness on the fit, or small roughness values. This is in agreement with the roughness estimation from the SEM images cross-section analysis.

In Fig. 8, Ψ and Δ data are presented for lithiation steps 0, 2 and 4, corresponding respectively to WO_3, $Li_{0.17}WO_3$ and $Li_{0.34}WO_3$. The parameters of the Tauc-Lorentz and Lorentz models reported in Table 4 were found by running the numerical curve-fitting procedure. When lithium content is increased, one can observe that the oscillations for both Ψ and Δ are greatly reduced. This dampening effect is stronger for longer wavelengths which is a direct consequence of the oscillator position of the Lorentz oscillator. The Lorentz oscillator is situated between 1.10 and 1.35 Ev, which corresponds to the wavelength range of 920–1125 nm. The longer wavelengths of the visible range are consequently more absorbed than the shorter ones leading to this well-known blue coloration of lithiated WO_3 films. The thickness of the as-deposited film has also been fitted and was found to be 1336 nm and appears to increase after each lithiation step. The optical band-gap is also included in the Tauc-Lorentz model (E_g) and appears to be stable upon lithiation.

In Fig. 9, the ellipsometric data Ψ and Δ are presented for lithiation steps 0, 2 and 4 corresponding respectively to $Mo_{0.10}W_{0.90}O_3$, $Li_{0.21}Mo_{0.10}W_{0.90}O_3$ and $Li_{0.42}Mo_{0.10}W_{0.90}O_3$. In this film, the dampening of the oscillation is relatively flat over the whole studied range (340–990 nm) when lithium is inserted. The numerical curve-fitting procedure was run to find the parameters of the Tauc-Lorentz and Lorentz models reported in Table 5. In this case, two Lorentz oscillators were used. One was deliberately positioned around the values found for pure WO_3, to simulate the absorption caused by its electronic states. The second one was found by fitting the curves and is associated to the additional electronic states created upon the insertion of molybdenum. The second oscillator, situated between 2,67 and 2,25 eV corresponding to the wavelength range of 465–550 nm, mixed with the first oscillator, leads to a flat dampening over the visible range and to the neutral colour observed in the previous section. The simulated thickness of the as-deposited film was found to be 1164 nm. Moreover, the simulated thickness of $Mo_{0.10}W_{0.90}O_3$ and its optical band-gap are respectively increasing and stable upon lithiation. Finally, for all samples, when the amount of inserted lithium increases, the new electronic states responsible for absorption increase too, which explains why the fitted Lorentz oscillators' strengths increase and why the oscillations are more and more damped.

The model fit parameters summarised in Tables 4 and 5 allowed to derive the real and complex part of the refractive index of both WO_3 and $Mo_{0.10}W_{0.90}O_3$ films, illustrated in Fig. 10. Concerning the real part, the derived refractive index of $Mo_{0.10}W_{0.90}O_3$ is lower than WO_3. This is explained by the pore volume fraction, which is larger for $Mo_{0.10}W_{0.90}O_3$. The Lorentz-Lorenz effective medium approximation

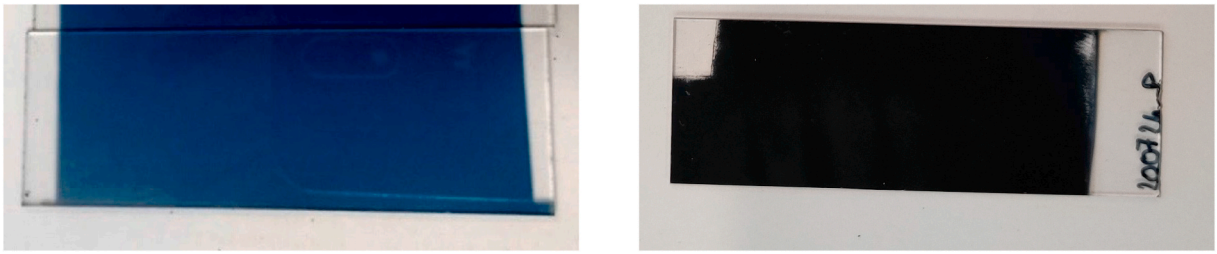

Fig. 5. Photograph of the WO_3 (left) and of the $Mo_{0.10}W_{0.90}O_3$ (right) coatings after two lithiation steps. The latter has a black colour neutral appearance.

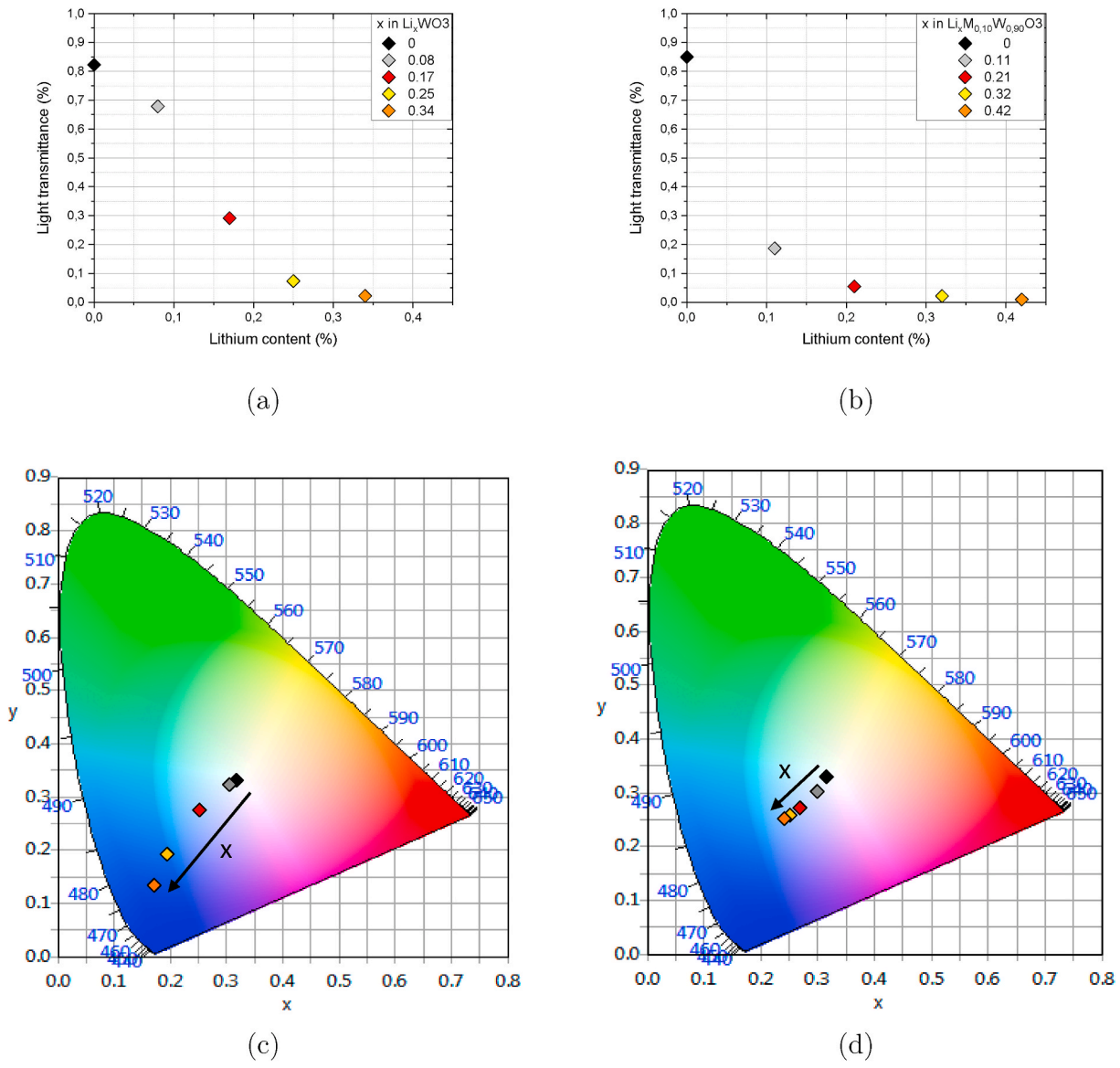

Fig. 6. (a), (b) light transmittance τ_v versus lithium content and (c), (d) x, y colour coordinates of the WO_3 (left) and $Mo_{0.10}W_{0.90}O_3$ (right) coatings as deposited on glass substrate and after successive lithiations steps. The arrows indicate the colour coordinates change direction, with increasing amount of lithium.

Table 4
Model fit parameters from VASE analysis of the WO_3 coating (as deposited on silicon substrate and for successive lithiations steps). The increasing oscillator strength at each lithiation step and the oscillator position of the model fit explain the oscillation dampening for longer wavelengths.

	Tauc-Lorentz				Lorentz			Results	
x in Li_xWO_3	A	E_0 [ev]	C[ev]	E_g [ev]	f	E_0 [ev]	Γ	ε_{inf}	Thickness [nm]
0	115.6	5.43	4.07	3.05	–	–	–	1.22	1336
0.08	66.7	5.00	1.67	3.03	0.32	1.10	1.75	1.92	1396
0.17	44.5	4.67	0.83	2.96	0.63	1.30	1.11	2.48	1409
0.25	48.2	4.67	1.08	3.04	1.26	1.33	1.17	2.45	1423
0.34	44.9	4.68	1.83	3.04	1.78	1.32	1.30	2.45	1434

(equation (8)) and ellipsometric results were used to determine the porosity of the as-deposited WO_3 and $Mo_{0.10}W_{0.90}O_3$ films, which was found to be respectively 14.9% and 21.8%. Baloukas et al. [29] used the same technique to derive the porosity of Mo-free and Li-free tungsten trioxide films (WO_3). They simultaneously measured the porosity with Rutherford back scattering and elastic recoil detection experiments and obtained similar results with both techniques. This difference of porosity can be explained by the deposition pressure. For a fully oxidised $Mo_{0.10}W_{0.90}O_3$ coating, a higher oxygen gas flow and a higher working pressure ($2.7{\cdot}10^{-2}$ mbar) than for pure WO_3 ($1.2{\cdot}10^{-2}$ mbar) were needed. At a higher deposition pressure, the mean free path of sputtered atoms is shorter leading to more porous coatings [30]. For both samples, the real part decreases with an increasing Li content while the opposite effect occurs for the complex part. For instance, at 550 nm, the as-deposited WO_3 has $n = 2.10$ and $k = 0$ whereas the $Li_{0.34}WO_3$ film has $n = 1.80$ and $k = 0.13$.

Table 5
Model fit parameters from VASE analysis of the $Mo_{0.10}W_{0.90}O_3$ coating, as deposited on silicon substrate and for successive lithiations steps.

x in $Li_xMo_{0.10}W_{0.90}O_3$	Tauc-Lorentz				Lorentz 1 and 2			Results	
	A	E_0	C	E_g	f	E_0	Γ	ε_{inf}	Thickness [nm]
0	88.3	5.49	4.11	3.04	–	–	–	1.39	1164
0.11	105.8	6.82	5.69	3.06	0.002	1.07	0.50	0	1292
					0.37	2.67	4.73		
0.21	97.3	7.44	5.69	3.06	0.5	1.34	4.00	0	1292
					0.54	2.25	3.93		
0.32	95.6	7.44	5.69	3.06	0.90	1.34	4.00	0	1314
					0.59	2.25	3.93		
0.42	93.9	7.46	5.72	3.06	1.01	1.34	3.44	0	1315
					0.72	2.25	3.93		

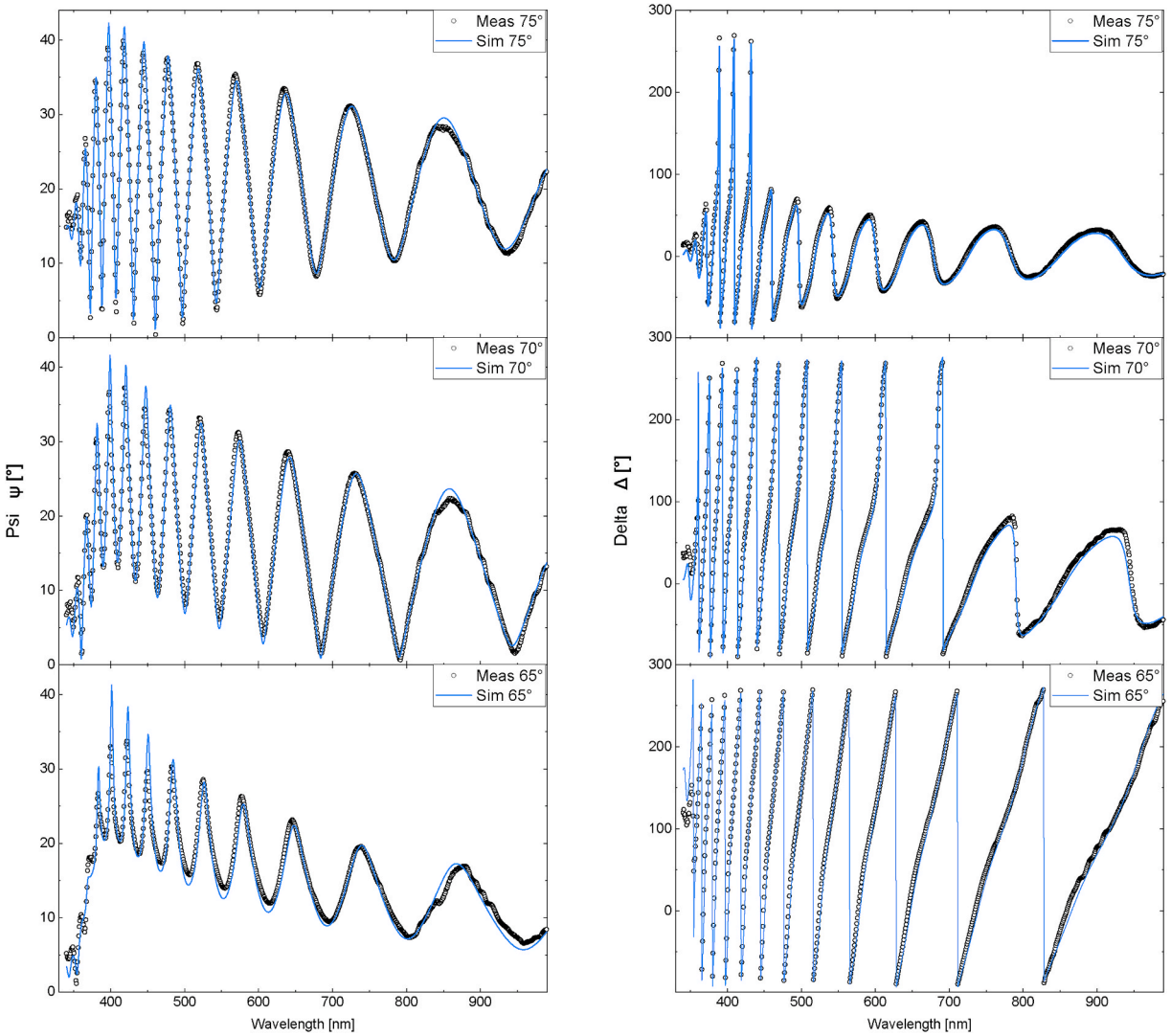

Fig. 7. Ellipsometric data, Ψ and Δ, measured (circles) and simulated (solid line) for the $Li_{0.08}WO_3$ sample at an angle of incidence of 75, 70 and 65°. After the numerical curve-fitting procedure, the measured and simulated data show excellent agreement.

4. Discussion

To analyse the experimental data on the ellipsometric angles Ψ and Δ, we used a straightforward model where the dispersion relation consists of the sum of Tauc-Lorentz and Lorentz oscillator dispersion laws. Both terms are associated with distinct physical phenomena. The Tauc-Lorentz dispersion law is associated with band-gap properties and describes the dispersion relation in the interband region, while the Lorentz oscillators are associated with electronic transitions with energy values lower than E_g. Before lithiation, nearly no absorption is observed for the as-deposited films for wavelengths longer than 400 nm in Fig. 4. Therefore, in absence of lithium, the dispersion relation can be described by the Tauc-Lorentz term only.

Upon lithiation, additional electronic transitions are available below the band-gap. The thin films become more and more absorbing and Lorentz oscillators with increasing oscillator strength are used to model

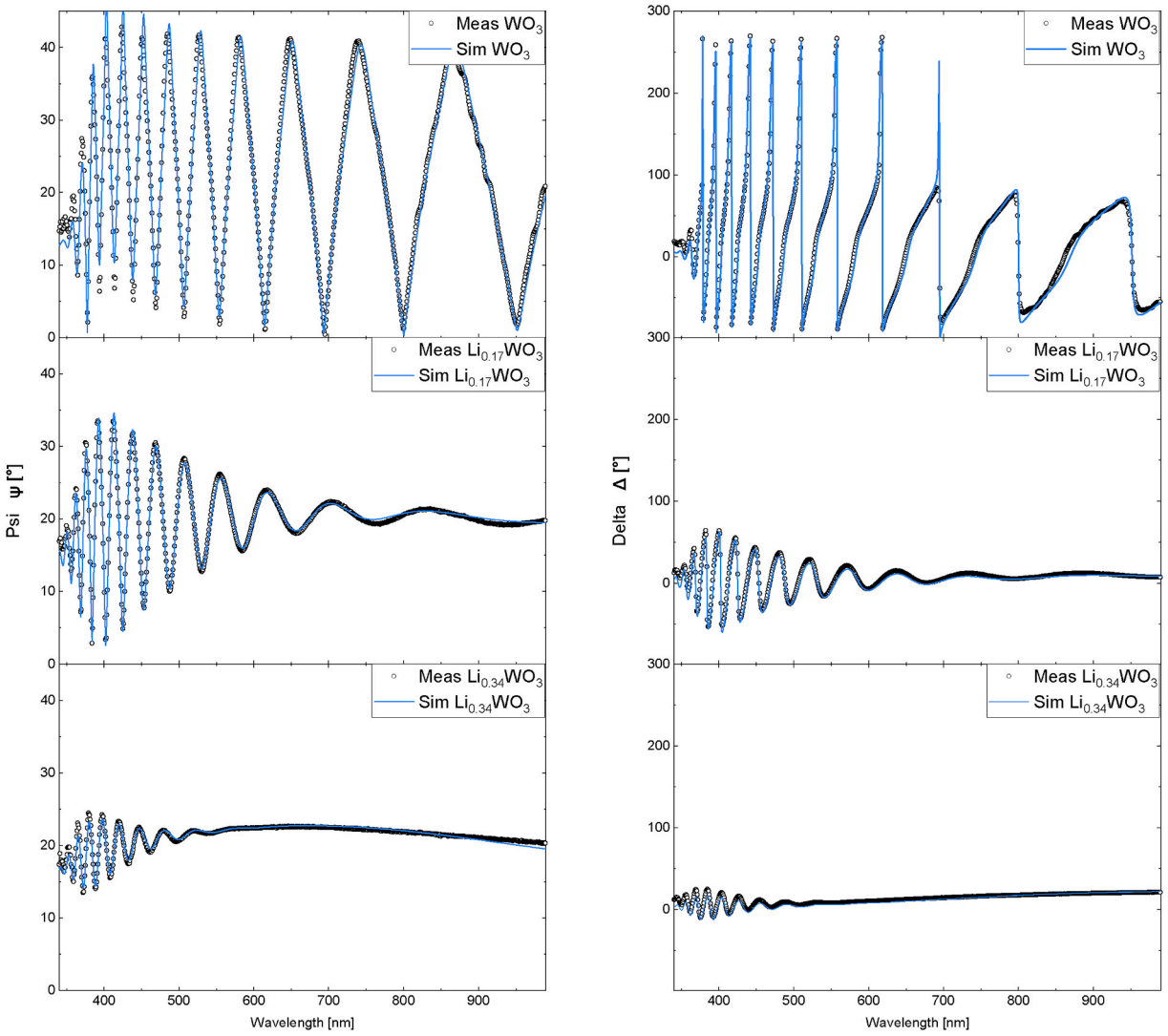

Fig. 8. Ellipsometric data, Ψ and Δ, measured (circles) and simulated (solid line) for the WO_3, $Li_{0.17}WO_3$, $Li_{0.34}WO_3$ samples at an angle of incidence of 75°. When lithium content increases, the oscillation of Ψ and Δ are increasingly damped especially for longer wavelengths.

this new feature. For WO_3 thin film, one Lorentz oscillator positioned around 1.3 eV, responsible of the blue hue, is associated with the reduction of W^{6+} to W^{5+}, typical for oxygen-deficient, hydrogenated or lithiated tungsten trioxide thin films [31,32]. For $Mo_{0.10}W_{0.90}O_3$, the previously occurring Lorentz oscillator positioned around 1.3 eV is used again, together with an additional Lorentz oscillator positioned around 2.3 eV. The latter is associated with the presence of Mo in the film. This is in agreement with the position of the absorption bands illustrated in Fig. 4 and the ones observed in literature [8]. To further explain these absorption bands and thus the tinting of lithiated WO_3 and $Mo_{0.10}W_{0.90}O_3$ thin films, it is useful to consider the structural and electronic properties of these materials.

In pure crystalline tungsten trioxide, each W^{6+} is octahedrally surrounded by six oxygen atoms [33], which is also the predominant atomic coordination for the short-range order of amorphous tungsten trioxide films [34]. As a consequence of the local electric field, the W5d orbitals split into partially delocalised t_{2g} and e_g levels [33,35]. A. Wach and al [36]. analysed this W5d orbital splitting by high resolution X-ray absorption spectroscopy, yielding an energy splitting of $\Delta oct \approx 3.6$ eV. This result is in agreement with the W5d level splitting of $\Delta oct \approx 4.0$ eV obtained by X-ray-absorption near-edge structure by Triana and al [34]. The band-gap (from O2p to Wt_{2g}) of lithium free or defect free tungsten oxide is wide enough to render it transparent [33,35], Vasilopoulou and al [31]. studied oxygen-deficient tungsten oxides WO_{3-x}. They suggest that a portion of the electrons coming from the oxygen vacancies is transferred to the initially empty $5d_{t2g}$ metallic orbitals, which are located partially at the edge of the conduction band and partially within the band-gap, near the Fermi level [31,37]. For oxygen-deficient metal oxides, such as tungsten and molybdenum oxides, a high density of occupied defect states within the band-gap has been observed in the valence-band photoemission spectra [38]. Moreover, N. Bondarenko and al [32]. showed some similarities between oxygen-deficient and lithiated tungsten oxides. Both exhibit the formation of polarons in WO_3 even though the polaron mobility is expected to be different. Due to these similarities, we can speculate that upon lithiation, a significantly high density of states is formed within the band-gap of Li_xWO_3, allowing new electronic transitions from these states to the ones situated at the edge of the conduction band. These new electronic transitions with energies around 1.3 eV would be responsible for the blue tint of lithiated WO_3 thin films.

In spite of a different atomic number ($Z_W = 74$ and $Z_{Mo} = 42$), Mo and W are group VI transition metals and their atomic radii are very close due to the lanthanum contraction. Due to these similarities, a large fraction of the W atoms can be substituted by Mo atoms [33]. As a consequence, it is expected that in $Mo_{0.10}W_{0.90}O_3$, most Mo^{6+} are octahedrally surrounded by six oxygen atoms and that the Mo4d orbitals

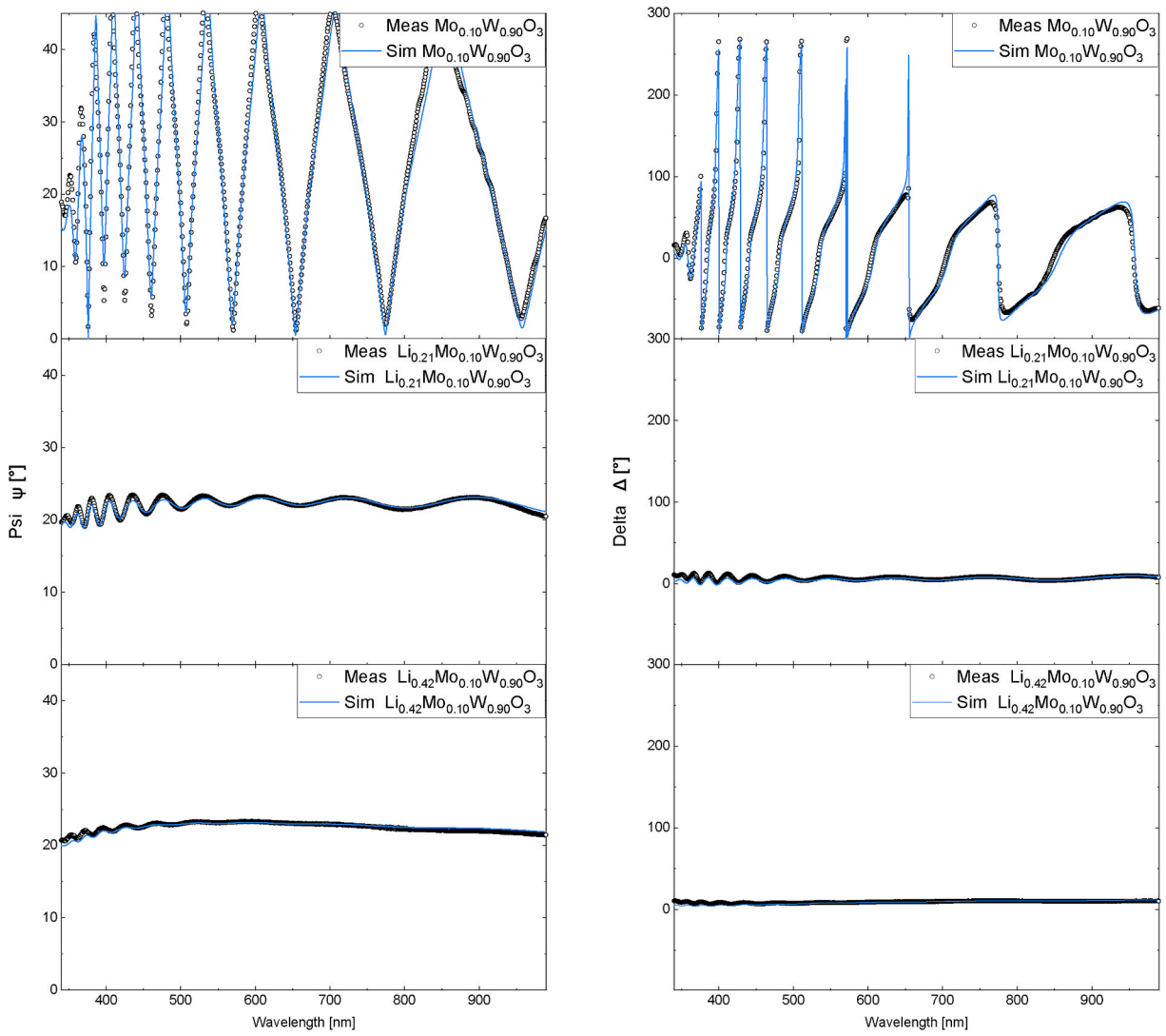

Fig. 9. Ellipsometric data, Ψ and Δ, measured (circles) and simulated for the fitted parameters (solid line) for the $Mo_{0.10}W_{0.90}O_3$, $Li_{0.21}Mo_{0.10}W_{0.90}O_3$, $Li_{0.42}Mo_{0.10}W_{0.90}O_3$ samples at an angle of incidence of 75°. When lithium content increases, the oscillation of Ψ and Δ are increasingly damped in the whole spectral range from 340 to 990 nm.

are split into t_{2g} and e_g states. When lithium is incorporated into $Mo_{0.10}W_{0.90}O_3$, new electronic transitions with energies around 2,3 eV arise. The combination of these two absorption bands centered around 1, 3 et 2,3 eV leads to the observed black colour neutral appearance.

5. Conclusion

Pure and Mo doped tungsten oxides were deposited by magnetron sputtering. Colour neutral tinting was obtained for $Mo_{0.10}W_{0.90}O_3$ by an in-vacuo lithiation technique. The dispersion relation of such coating has been modeled as the sum of one Tauc-Lorentz term and two Lorentz oscillators. The Tauc-Lorentz term is associated with band-gap properties and describes the dispersion relation in the interband region. The Lorentz oscillator positioned around 1.3 eV is associated with the reduction of W^{6+} to W^{5+} by lithium incorporation. These new electronic transitions occur from states formed within the band gap to states situated at the edge of the conduction band. The Lorentz oscillator positioned around 2.3 eV is associated with additional states in the band-gap due to the presence of Mo in the lithiated film. The refractive index and the extinction coefficient were derived with this proposed model for lithiated WO_3 and $Mo_{0.10}W_{0.90}O_3$. These n and k data can be used for the modelling of electrochromic devices. When a sufficient amount of Li is incorporated inside $Mo_{0.10}W_{0.90}O_3$, τ_e and τ_v can be highly reduced from 83.3% to 2.7% and from 85.0% to 0.9% respectively. Such a large modulation of both the visible and solar energy transmittance are of interest to provide glare and overheating protection for smart window applications [39].

CRediT authorship contribution statement

Maxime Lagier: Conceptualization, Investigation, Visualization, Writing – original draft. **Aurélien Bertinotti:** Investigation, Visualization, Writing – review & editing. **Olivia Bouvard:** Investigation, Visualization, Writing – review & editing. **Luc Burnier:** Investigation, Visualization, Writing – review & editing. **Andreas Schüler:** Conceptualization, Supervision, Writing – review & editing.

Declaration of competing interest

The authors declare that they have no known competing financial interests or personal relationships that could have appeared to influence the work reported in this paper.

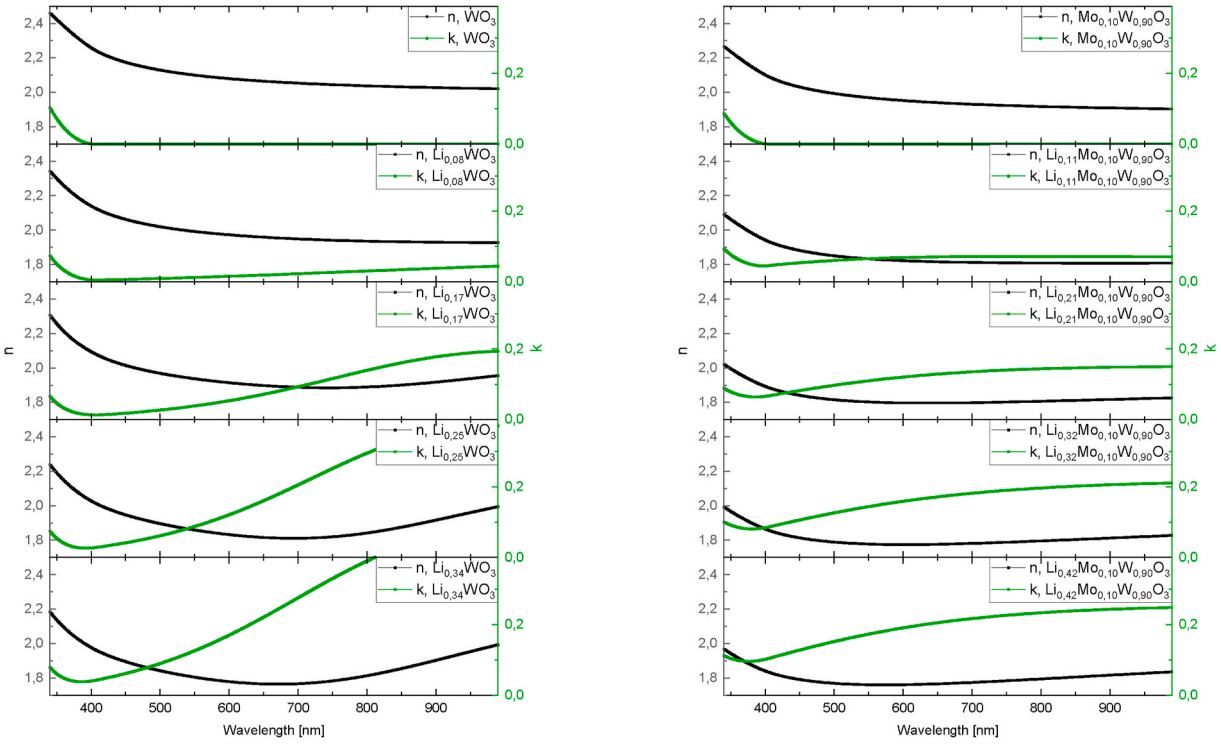

Fig. 10. refractive index and extinction coefficient of the WO_3 (left) and $Mo_{0.10}W_{0.90}O_3$ (right) coatings as deposited on silicon substrate and after successive lithiations steps.

Acknowledgements

This research project is financially supported by the Swiss Innovation Agency Innosuisse as part of the Swiss Competence Centre for Energy Research SCCER FEEB&D. We are grateful to Gregoire Baroz for SEM assistance, to Yann Lavanchy for the ellipsometer training and to Wen Hua Bi for XRD measurements. Furthermore, we gratefully acknowledge Pierre Loesch and the PLTE platform for technical support. In addition, we would like to thank Barbara Smith for proof-reading of the manuscript.

References

[1] J.S.E.M. Svensson, C.G. Granqvist, Electrochromic tungsten oxide films for energy efficient windows, Sol. Energy Mater. 11 (1) (October 1984) 29–34.
[2] Roger J. Mortimer, Organic electrochromic materials, Electrochim. Acta 44 (18) (May 1999) 2971–2981.
[3] Vyomesh R. Buch, Kumar Chawla Amit, K Rawal Sushant, Review on electrochromic property for WO3 thin films using different deposition techniques, Mater. Today: Proceedings 3 (6) (January 2016) 1429–1437.
[4] Miguel A. Arvizu, Gunnar A. Niklasson, Claes-Göran Granqvist, Electrochromic $W^{1-x-y}Ti_xMo_yO^3$ thin films made by sputter deposition: large optical modulation, good cycling durability, and approximate color neutrality, Chem. Mater. 29 (5) (2017) 2246–2253.
[5] K. von Rottkay, M. Rubin, S.J. Wen, Optical indices of electrochromic tungsten oxide 306 (1) (August 1997) 10–16.
[6] G. Beydaghyan, G. Bader, P.V. Ashrit, Electrochromic and morphological investigation of dry-lithiated nanostructured tungsten trioxide thin films, Thin Solid Films 516 (8) (February 2008) 1646–1650.
[7] Guangzhong Yuan, Chenzheng Hua, Li Huang, Christophe Defranoux, Basa Peter, Yong Liu, Chenlu Song, Gaorong Han, Optical characterization of the coloration process in electrochromic amorphous and crystalline WO^3 films by spectroscopic ellipsometry, Appl. Surf. Sci. 421 (November 2017) 630–635.
[8] A. Pennisi, F. Simone, C.M. Lampert, Electrochromic properties of tungsten-molybdenum oxide electrodes, Sol. Energy Mater. Sol. Cells 28 (3) (1992) 233–247.
[9] Lilia Kondrachova, Benjamin P. Hahn, Ganesh Vijayaraghavan, Ryan D. Williams, Keith J. Stevenson, Cathodic electrodeposition of mixed molybdenum tungsten oxides from peroxo-polymolybdotungstate solutions, Langmuir 22 (25) (2006) 10490–10498.
[10] Sijie Xie, Zhijie Bi, Yongbo Chen, Xiaoli He, Xiangxin Guo, Xiangdong Gao, Xiaomin Li, Electrodeposited Mo-doped WO^3 film with large optical modulation and high areal capacitance toward electrochromic energy-storage applications, Appl. Surf. Sci. 459 (November 2018) 774–781.
[11] Olivia Bouvard, Luc Burnier, Maxime Lagier, Andreas Schüler, Strong coloration of nanoporous tungsten oxides by in-vacuo lithiation for all-solid-state electrochromic devices, Manuscript submitted to Thin Solid Films (2021) 138700. https://doi.org/10.1016/j.tsf.2021.138700. In preparation.
[12] Saes getters, Alkali Metal Dispensers, 2007.
[13] Matthias Töwe, Photoelectron Spectroscopy Studies of Carbon Based Fusion Reactor Materials, PhD thesis, University of Basel, 2003.
[14] A. Gremaud, J. Geng, A. Schuler, G. Indlekofer, P. Oelhafen, Metal to insulator transition of K-Sn Zintl system investigated by ultraviolet photoelectron spectroscopy, Helv. Phys. Acta 71 (1998) 17–18.
[15] R. Steiner, P. Oelhafen, G. Reber, A. Romanyuk, Experimental determination of spectral and angular dependent optical properties of insulating glasses, Proc. of CISBAT, EPFL (2005) 441–446, www. glassdbase.ch/glassdocs/2121-CISBAT2005_Oelhafen1Logo. pdf.
[16] Olivia Bouvard, L. Burnier, P. Oelhafen, A. Tonin, P. Wüst, F. Sidler, G. Zweifel, A. Schüler, Solar heat gains through train windows: a non-negligible contribution to the energy balance, Energy Efficiency 11 (6) (2018) 1397–1410.
[17] British Standards Institution, Glass in Building: Determination of Luminous and Solar Characteristics of Glazing, British Standards Institution, 1998.
[18] V. Hody-Le Caër, Estelle De Chambrier, Stefan Mertin, Martin Joly, Marie Schaer, J.-L. Scartezzini, Andreas Schüler, Optical and morphological characterisation of low refractive index materials for coatings on solar collector glazing, Renew. Energy 53 (2013) 27–34.
[19] Martin Joly, Olivia Bouvard, Thomas Gascou, Yannik Antonetti, Python Martin, Marina A Gonzalez Lazo, Pierre Loesch, Aïcha Hessler-Wyser, Andreas Schüler, Optical and structural analysis of sol–gel derived Cu–Co–Mn–Si oxides for black selective solar nanocomposite multilayered coatings, Sol. Energy Mater. Sol. Cell. 143 (2015) 573–580.
[20] Jellison Ge Jr., F.A. Modine, Parameterization of the optical functions of amorphous materials in the interband region, Appl. Phys. Lett. 69 (3) (1996) 371–373.
[21] R Alan May, Lilia Kondrachova, Benjamin P. Hahn, Keith J. Stevenson, Optical constants of electrodeposited mixed molybdenum- tungsten oxide films determined by variable-angle spectroscopic ellipsometry, J. Phys. Chem. C 111 (49) (2007) 18251–18257.
[22] J.D. Jackson, Classical Electrodynamics, 1975.
[23] A. Vadim, Markel. Introduction to the Maxwell Garnett approximation: Tutorial, JOSA A 33 (7) (July 2016) 1244–1256.
[24] C. Millán, C. Santonja, M. Domingo, R. Luna, M. Á Satorre, An experimental test for effective medium approximations (EMAs) - porosity determination for ices of astrophysical interest, Astron. Astrophys. 628 (A63) (August 2019).
[25] Andreas Schüler, Christoph Ellenberger, Oelhafen Peter, Christian Haug, Rüdiger Brenn, Optical properties of titanium containing amorphous hydrogenated carbon films (a-C:H/Ti), J. Appl. Phys. 87 (9) (April 2000) 4285–4292.

[26] S. Sawada, G.C. Danielson, Optical indices of refraction of WO^3, Phys. Rev. 113 (4) (February 1959) 1008–1013.
[27] Luc Lajaunie, Florent Boucher, Remi Dessapt, Philippe Moreau, Strong anisotropic influence of local-field effects on the dielectric response of α-MoO_3, Phys. Rev. B 88 (11) (2013) 115141.
[28] J. Scarminio, A. Urbano, B. Gardes, The beer-lambert law for electrochromic tungsten oxide thin films, Mater. Chem. Phys. 61 (2) (1999) 143–146.
[29] B. Baloukas, J.M. Lamarre, L. Martinu, Electrochromic interference filters fabricated from dense and porous tungsten oxide films, Sol. Energy Mater. Sol. Cell. 95 (3) (March 2011) 807–815.
[30] W.D. Westwood, Porosity in sputtered platinum films, J. Vac. Sci. Technol. 11 (1) (1974) 466–471.
[31] M. Vasilopoulou, A. Soultati, D.G. Georgiadou, T. Stergiopoulos, L.C. Palilis, S. Kennou, N.A. Stathopoulos, D. Davazoglou, P. Argitis, Hydrogenated under-stoichiometric tungsten oxide anode interlayers for efficient and stable organic photovoltaics, J. Mater. Chem. 2 (6) (2014) 1738–1749.
[32] Nina Bondarenko, Olle Eriksson, V Skorodumova Natalia, Polaron mobility in oxygen-deficient and lithium-doped tungsten trioxide, Phys. Rev. B 92 (16) (2015) 165119.
[33] Liang Zhou, Jie Zhu, Meihua Yu, Xiaodan Huang, Zhen Li, Yunhua Wang, Chengzhong Yu, $Mo_xW^{1-x}O^3 \cdot 0.33\ H^2O$ solid solutions with tunable band gaps, J. Phys. Chem. C 114 (49) (2010) 20947–20954.
[34] Carlos A. Triana, C. Moyses Araujo, Rajeev Ahuja, Gunnar A. Niklasson, Tomas Edvinsson, Disentangling the intricate atomic short-range order and electronic properties in amorphous transition metal oxides, Sci. Rep. 7 (1) (2017) 1–12.
[35] Yuping He, Zhenyu Wu, Limin Fu, Chaorong Li, Yanming Miao, Li Cao, Haiming Fan, Bingsuo Zou, Photochromism and size effect of WO^3 and WO^3-TiO^2 aqueous sol, Chem. Mater. 15 (21) (2003) 4039–4045.
[36] Wach Anna, Wojciech Błachucki, Joanna Czapla-Masztafiak, Daniel Luis Abreu Fernandes, Dariusz Banaś, Klaudia Wojtaszek, Krzysztof Tyrała, M Kwiatek Wojciech, Sa Jacinto, Jakub Szlachetko, In situ observation of charge transfer and crystal field formation with high energy resolution x-ray spectroscopy during temperature programmed oxidation, Phys. Chem. Chem. Phys. 22 (2020) 14731–14735, 26.
[37] John B. Goodenough, The two components of the crystallographic transition in vo2, J. Solid State Chem. 3 (4) (1971) 490–500.
[38] Mark T. Greiner, Zheng-Hong Lu, Thin-film metal oxides in organic semiconductor devices: their electronic structures, work functions and interfaces, NPG Asia Mater. 5 (7) (2013) e55–e55.
[39] Esteban Damián Avendaño Soto, Electrochromism in nickel-based oxides: coloration mechanisms and optimization of sputter-deposited thin films, PhD thesis, Acta Universitatis Upsaliensis, 2004.